CrossMark

On the structure of streamwise wall-shear stress fluctuations in turbulent channel flows

Cheng Cheng[1], Weipeng Li[1],†, Adrián Lozano-Durán[2] and Hong Liu[1]

[1]School of Aeronautics and Astronautics, Shanghai Jiao Tong University, Shanghai 200240, China

[2]Center for Turbulence Research, Stanford University, Stanford, CA 94305, USA

A growing body of studies in wall-bounded turbulence has shown that the generation of wall-shear stress fluctuations is directly connected with outer-layer large-scale motions. In the present study, we investigate the scale-based structures of the streamwise wall-shear stress fluctuations (τ'_x) in turbulent channel flows at different Reynolds numbers. The wall-shear stress structures are identified using a two-dimensional clustering methodology, and two indispensable factors, scale and sign, are considered for the analysis. The structures are classified into positive and negative families according to the sign of τ'_x. The statistical properties of the structures, including geometrical characteristics, spatial distribution, population density, fluctuating intensity, and correlations with outer motions are comprehensively investigated. Particular attention is paid to the asymmetries between positive and negative structures and their connection with wall-attached energy-containing eddies. In virtue of our results, only the large-scale structures of negative τ'_x contain the footprints of the inactive part of wall-attached eddies populating the logarithmic region.

Key words: boundary layer structure, turbulent boundary layers

1. Introduction

The ability to understand and predict the wall-shear stress in wall-bounded turbulence is pursued in aerodynamic/hydrodynamic design of modern aircraft and ships, among many engineering applications. The wall-shear stress can be decomposed into mean and fluctuating components, i.e. $\tau_w = \overline{\tau_w} + \tau'_w$. Although many studies have focused on the properties of the mean wall-shear stress, such as its Reynolds number dependence (Nagib, Chauhan & Monkewitz 2007; Chauhan, Monkewitz & Nagib 2009; Schlatter & Örlü 2010), its physical-informed decomposition and connection with the statistical quantities across the wall layer (Fukagata, Iwamoto & Kasagi 2002; Renard & Deck 2016; Yoon *et al.* 2016; Modesti *et al.* 2018; Fan, Cheng & Li 2019*a*; Fan, Li & Pirozzoli 2019*b*; Li *et al.* 2019) and active/passive control approaches (Gose *et al.* 2018; Yao, Chen & Hussain 2018; Li & Liu 2019; Yao & Hussain 2019), to date, very few works have investigated the features of wall-shear stress fluctuations and their associated dynamics. Despite this lack of analysis, wall-shear stress fluctuations are of importance for noise radiation, structural

vibration, drag generation and wall heat transfer, among others (Choudhari & Khorrami 2007; Diaz-Daniel, Laizet & Vassilicos 2017; Zhang *et al.* 2017; Bae *et al.* 2018).

First laboratory experiments were incapable of measuring the instantaneous wall-shear stress with enough accuracy to produce meaningful signals. Researchers reported that the intensity of the wall-shear stress fluctuations were not sensitive to the Reynolds number within the measurement uncertainties (Eckelmann 1974; Chambers, Murphy & McEligot 1983; Madavan, Deutsch & Merkle 1985; Karlsson & Johansson 1986; Alfredsson *et al.* 1988). For instance, Alfredsson *et al.* (1988) suggested that the root mean squared value of streamwise wall-shear stress fluctuations follows $\tau'_{x,rms} = 0.4\overline{\tau_x}$, where $\overline{\tau_x}$ is the mean component of the streamwise wall-shear stress. However, recent studies using both direct numerical simulations (DNS) and experiments have shown that $\tau'_{x,rms}$ is actually sensitive to changes in the Reynolds number (Fischer, Jovanović & Durst 2001; Abe, Kawamura & Choi 2004; Hu, Morfey & Sandham 2006; Große & Schröder 2009; Schlatter & Örlü 2010; Örlü & Schlatter 2011; Yang & Lozano-Durán 2017). Schlatter & Örlü (2010) proposed an empirical correlation to predict the dependence of $\tau'_{x,rms}$ on the friction Reynolds number, i.e. $\tau'_{x,rms}/\overline{\tau_x} = 0.298 + 0.018 \ln(Re_\tau)$, where $Re_\tau = u_\tau \delta/\nu$, u_τ is the friction velocity, ν is the kinematic viscosity and δ is the boundary-layer thickness (or channel half-height). The Reynolds number dependence of $\tau'_{x,rms}$ suggests that large-scale energy-containing motions populating the logarithmic and outer regions in high-Reynolds-number wall turbulence have non-negligible influences on the near-wall dynamics and, hence, on the wall friction (Abe *et al.* 2004; Örlü & Schlatter 2011; de Giovanetti, Hwang & Choi 2016; Renard & Deck 2016; Baidya *et al.* 2019; Fan *et al.* 2019*a*,*b*).

The characteristics of organized turbulent motions in the logarithmic and outer regions and their interactions with the near-wall dynamics have been the focus of multiple studies. Large-scale motions (LSM) and very large-scale motions (VLSM) have been identified in high-Reynolds-number pipes (Kim 1999; Wu, Baltzer & Adrian 2012), channels (Del Álamo *et al.* 2004, 2006; Lozano-Durán & Jiménez 2014*a*) and zero-pressure-gradient turbulent boundary layers (Wark & Nagib 1991; Sillero, Jiménez & Moser 2013). Further studies also revealed that these energy-containing motions exert a pronounced influence on the near-wall turbulent intensities (Abe *et al.* 2004; Hutchins & Marusic 2007; Mathis, Hutchins & Marusic 2009; Marusic, Mathis & Hutchins 2010; Ganapathisubramani *et al.* 2012; Mathis *et al.* 2013; Hu & Zheng 2018; Agostini & Leschziner 2019*b*) in the form of superposition and modulation of the near-wall flow velocities. The former refers to the footprint of large-scale fluctuations on the near-wall turbulence, while the latter is the intensity amplification or attenuation of near-wall small-scale structures by the outer motions. Mathis *et al.* (2013) modelled the integrated effects of superposition and modulation in the wall-shear stress as

$$\tau'^{+}_w(y^+) = \tau'^{*}_w(y^+)\left\{1 + \beta_u u^+_{OL}(y^+_O)\right\} + \alpha_u u^+_{OL}(y^+_O), \tag{1.1}$$

where τ'^{+}_w is the wall-shear stress fluctuations scaled by viscous units, y^+ is the wall-normal height scaled by viscous units, τ'^{*}_w is the near-wall universal signal without the outer influences, u^+_{OL} denotes the large-scale streamwise turbulent intensities at the centre of the logarithmic region y^+_O, and α_u, β_u are the superposition and modulation coefficients, respectively. Mathis *et al.* (2013) emphasized that the superposition and modulation in (1.1) are essential for the generation of wall-shear stress fluctuations. The modulation model has also been successful in predicting near-wall velocity fluctuations by using fluid properties in the outer region for the velocity fluctuations (Marusic *et al.* 2010). Note that in (1.1), positive and negative values of u^+_{OL} have equally weighted contributions to the near-wall fluctuations. However, the presence of nonlinear interactions and energy transfer

between inner and outer scales suggests that this expression might not capture fully the generation of wall stress. Agostini & Leschziner (2016*a*,*b*, 2018, 2019*a*) stated that the modulation of near-wall streamwise velocity fluctuations by outer LSM is exceedingly asymmetric, i.e. the amplification caused by positive outer LSM is much stronger than the attenuation caused by negative ones. Recently, Howland & Yang (2018) argued that the amplification and attenuation of the near-wall turbulence by LSM might follow different mechanisms. Moreover, Kawata & Alfredsson (2018) and Cho, Hwang & Choi (2018) observed inverse energy transfer from small-scale motions to LSM in the vicinity of the wall. Therefore, two indispensable factors should be considered to investigate the mechanism of the near-wall turbulence, i.e. the scale and sign of the motions involved, which is focus of the present study.

The attached-eddy hypothesis provides a conceptual model describing the multiscale nature of fluid motions in wall-bounded turbulence, which was first proposed by Townsend (1976). In the model, it is conjectured that the logarithmic layer is populated by a collection of randomly distributed energy-containing motions (or eddies) with their roots attached to the 'wall' (the near-wall region). Based on Townsend's attached-eddy model, the turbulent intensities can be predicted as

$$\overline{u'^2}^+ = B_1 - A_1 \ln(y/\delta), \tag{1.2a}$$

$$\overline{w'^2}^+ = B_2 - A_2 \ln(y/\delta), \tag{1.2b}$$

$$\overline{v'^2}^+ = B_3, \tag{1.2c}$$

where u', v' and w' are the streamwise, wall-normal and spanwise velocity fluctuations, respectively, and A_i ($i = 1, 2$) and B_j ($j = 1, 2, 3$) are constants. This model has been extended and developed by Perry & Chong (1982), Perry, Henbest & Chong (1986), Perry & Marusic (1995), Marusic (2001), Meneveau & Marusic (2013), Woodcock & Marusic (2015) and Mouri (2017), to name a few, where other works have complemented the original picture proposed by Townsend (Mizuno & Jiménez 2011; Davidson, Nickels & Krogstad 2006; Dong *et al.* 2017; Lozano-Durán & Bae 2019; Hu, Yang & Zheng 2020). For more details, the reader is referred to a recent review work by Marusic & Monty (2019). Many observations favour the existence of the wall-attached eddies, such as the logarithmic increase of the near-wall streamwise velocity fluctuations with the Reynolds number (Marusic & Kunkel 2003; Hoyas & Jiménez 2006), the emergence of k_x^{-1} (k_x is the streamwise wavenumber) region in the spectra of streamwise velocity (Nickels *et al.* 2005), and the linear growth of spanwise integral length of the energy-containing motions with the distance to the wall (Tomkins & Adrian 2002; Del Álamo *et al.* 2004; Hoyas & Jiménez 2006; Lozano-Durán, Flores & Jiménez 2012; Lee & Moser 2015; Cheng *et al.* 2019).

Recently, Diaz-Daniel *et al.* (2017) proposed a generalized attached-eddy model to describe the generation of wall-shear stress fluctuations and investigated the linkage between the filtered wall-shear stress fluctuations and the second-order structure functions of velocity fluctuations at a given wall-normal location. Yang & Lozano-Durán (2017) reported that the generation of wall-shear stress fluctuations can be interpreted as a momentum cascade across wall-attached eddies of different scales. Pan & Kwon (2018) found that the conditionally averaged velocities in the proximity of the positive and negative extremes of friction events in the turbulent boundary layer exhibit disparate patterns, implying different mechanisms between the extremes with the structures populating above the wall. Baidya *et al.* (2019) measured the instantaneous

Case	Re_τ	$L_x(h)$	$L_y(h)$	$L_z(h)$	Δx^+	Δz^+	Δy_{min}^+	Δy_{max}^+	N_F
*Re*550	547	8π	2	4π	13.4	6.8	0.04	6.7	142
*Re*950	934	8π	2	3π	11.5	5.7	0.03	7.6	21
*Re*2000	2009	8π	2	3π	12.3	6.2	0.32	8.9	10

TABLE 1. Parameters of the DNS. Here, L_x, L_y and L_z are the sizes of the computational domain in the streamwise, wall-normal and spanwise direction, respectively. Here, Δx^+ and Δz^+ denote the streamwise and spanwise grid resolutions, respectively, in inner units. Here, Δy_{min}^+ and Δy_{max}^+ are the finest and coarsest resolution in the wall-normal direction, respectively. Here, N_F is the number of flow fields used to accumulate statistics.

wall-shear stress in high-Reynolds-number pipes and boundary layers and found that the energy-containing motions are stochastically coherent with skin-friction events. In the present work, we aim to analyse the structure of the wall-shear stress fluctuations and to assess the relationship between the skin-friction events with the wall-attached eddies. Special emphasis is placed on the length scale and sign of the flow motions contributing to the wall-shear stress generation.

The paper is organized as follows. In §§ 2 and 3, the DNS database and the method for structure identification are introduced. In § 4, the statistical properties of wall-shear stress structures, including geometrical characteristics, spatial distribution, population density, fluctuating intensity and correlations with outer streamwise velocity motions are investigated. Finally, concluding remarks are summarized in § 5.

2. DNS database

The DNS database used in the present study has been extensively validated by Jiménez and coworkers (Del Álamo & Jiménez 2003; Del Álamo *et al.* 2004; Hoyas & Jiménez 2006; Lozano-Durán *et al.* 2012; Lozano-Durán & Jiménez 2014*b*). Three cases at $Re_\tau = $ 545, 934 and 2009 are selected and named as *Re*550, *Re*950 and *Re*2000, respectively. The DNS database was originally built in Del Álamo & Jiménez (2003), Del Álamo *et al.* (2004) and Hoyas & Jiménez (2006). Details of the parameter settings are listed in table 1. Hereafter, x, y and z stand for the streamwise, wall-normal and spanwise directions, respectively. The computational domains in table 1 are large enough to resolve the LSM and VLSM (Guala, Hommema & Adrian 2006; Hutchins & Marusic 2007; Hwang 2015).

In this study, we focus on the streamwise wall-shear stress fluctuations, τ_x'. The root mean squared value of τ_x' is normalized by its mean component ($\overline{\tau_x}$) and expressed as

$$\tau_{x,rms}^+ = \frac{\tau_{x,rms}'}{\overline{\tau_w}}. \tag{2.1}$$

The variations of $\tau_{x,rms}^+$ as a function of Re_τ are shown in figure 1. Previous estimations of $\tau_{x,rms}^+$ using DNS of channel flows (Hu *et al.* 2006) and DNS of zero-pressure-gradient turbulent boundary layers (Schlatter & Örlü 2010) are also included in the plot for comparison. The results show that $\tau_{x,rms}^+$ increases with Re_τ, implying that the LSM have an influence on the skin-friction events (Örlü & Schlatter 2011; Mathis *et al.* 2013). In our present results, the Reynolds number dependence of $\tau_{x,rms}^+$ is well fitted by the empirical formula, $\tau_{x,rms}^+ = 0.292 + 0.018 \ln(Re_\tau)$. The data of Hu *et al.* (2006) also collapse with
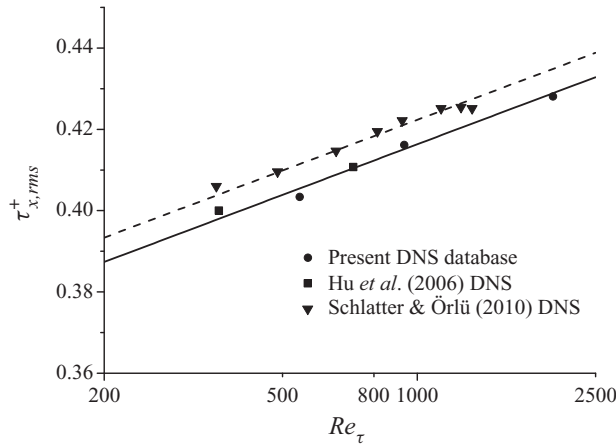
FIGURE 1. Variations of $\tau^+_{x,rms}$ as a function of Re_τ. The solid line is the empirical formula defined by $\tau^+_{x,rms} = 0.292 + 0.018\ln(Re_\tau)$ for channel flows. The dashed line is the empirical formula defined by $\tau^+_{x,rms} = 0.298 + 0.018\ln(Re_\tau)$ for zero-pressure-gradient turbulent boundary layers (Schlatter & Örlü 2010).
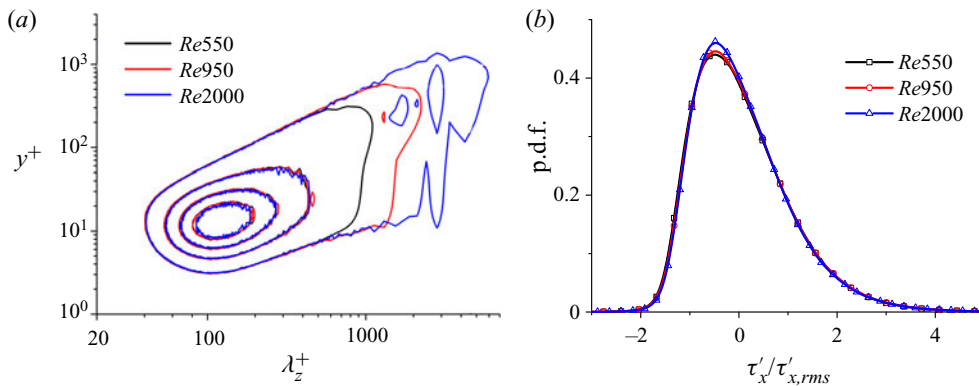

FIGURE 2. (*a*) The spanwise premultiplied spectra of the streamwise velocity fluctuations. Contour lines are 0.2, 0.4, 0.6 and 0.8 of the maximum. (*b*) The probability density functions (p.d.f.s) of normalized streamwise wall-shear fluctuations ($\tau'_x/\tau'_{x,rms}$).

our empirical formula, which is similar to the estimation given by Schlatter & Örlü (2010) for turbulent boundary layers.

Figure 2(*a*) shows the spanwise premultiplied spectra of the streamwise velocity fluctuations. It can be seen that the spectra span from $\lambda^+_z \approx O(10)$ to $\lambda_z \approx O(h)$, where λ_z denotes the spanwise wavelength. The small scales of the spectra in the near-wall region ($y^+ \le 100$) scale well in viscous units. As the Reynolds number increases, the footprint of the LSM penetrates deep into the near-wall region and become apparent at large wavelengths, suggesting that LSM may affect the generation of the skin-friction events. Figure 2(*b*) shows the p.d.f.s of normalized streamwise wall-shear fluctuation ($\tau'_x/\tau'_{x,rms}$). The p.d.f.s are asymmetric in shape and positively skewed. This outcome highlights that the high- and low-speed skin-friction events are organized in fundamentally different manners, which will be investigated in the following sections.

3. Structure identification method

We follow a clustering methodology to identify the structure of regions of intense τ'_x. The method has been used to identify three-dimensional turbulent structures in previous studies (Moisy & Jiménez 2004; Del Álamo *et al.* 2006; Lozano-Durán *et al.* 2012; Lozano-Durán & Jiménez 2014a; Dong *et al.* 2017; Hwang & Sung 2018, 2019; Osawa & Jiménez 2018; Cardesa *et al.* 2019). We adapt the methodology to compute two-dimensional structures in order to analyse the fields of τ'_x. A brief description of the approach is given as follows.

(i) The grid points at the wall satisfying

$$\tau'_x < -\alpha \tau'_{x,rms} \tag{3.1}$$

or

$$\tau'_x > \alpha \tau'_{x,rms} \tag{3.2}$$

are marked, where α is a positive threshold value. Criteria (3.1) and (3.2) extract negative and positive intense skin-friction events, respectively.

(ii) The grid points marked in step (i) which are contiguous in space are connected into individual structures using the four orthogonal neighbours connectivity rule (Rosenfeld & Pfaltz 1966).

(iii) The spatially connected regions in step (ii) are defined as τ'_x structures. The bounding rectangle aligned with the Cartesian grid of each individual structure has length l_x and width l_z, which are chosen as the characteristic length scales of the structures.

Hereafter, we denote the structures satisfying (3.1) and (3.2) as NF_s and PF_s, respectively. Only structures with an area larger than 30×30 viscous units are taken into consideration to avoid artefact due to the limited grid resolution of the DNS database (Del Álamo *et al.* 2006; Lozano-Durán *et al.* 2012). As in previous work, we follow the percolation theory to determine the value of α (Moisy & Jiménez 2004; Del Álamo *et al.* 2006; Lozano-Durán *et al.* 2012; Lozano-Durán & Jiménez 2014a; Dong *et al.* 2017; Hwang & Sung 2018, 2019; Osawa & Jiménez 2018; Cheng *et al.* 2020). Figure 3 shows the percolation diagram for NF_s and PF_s, when α varies from 0.05 to 2.5. Dash-dotted lines represent the area fractions (A/A_m) of the structures, where $A = \sum (l_x l_z)$ is the sum of all the individual areas of the structures for a given α, and A_m is the maximum A over $0.05 \leq \alpha \leq 2.5$. Solid lines represent the number fraction (N/N_m), where N is the total number of the structures identified for a given α and N_m is the maximum N over $0.05 \leq \alpha \leq 2.5$.

We take figure 3(*a*) as an example. When $\alpha < 0.2$, $A/A_m \approx 1$, most grid points extracted in step (i) are connected into a single structure. Percolation transition occurs in the range of $0.2 \lesssim \alpha \lesssim 1.3$, where A/A_m decreases gradually with increasing α. When $\alpha > 1.3$, the identification process yields fragmentary structures corresponding to very strong friction regions. The variations of N/N_m are different. When $\alpha < 1.3$, N/N_m increases with α as new structures appear. The number of identified structures attains the maximum at $\alpha \approx 1.3$. Similar features can be found in the percolation diagram of PF_s, as shown in figure 3(*b*). According to the percolation transition shown in figure 3, we choose $\alpha = 0.5$ (vertical lines in figure 3). Nonetheless, the results discussed in the remainder of the paper are qualitatively similar for values of α in the range of $0.4 \leq \alpha \leq 0.7$ (see the Appendix).

With $\alpha = 0.5$, the total number, area and area fraction of the structures (NF_s and PF_s) are summarized in table 2. The area fraction is defined by $A_f = A/(N_F A_w)$, where $A_w = 2L_x \times L_z$ represents the total area of the upper and lower walls and N_F is the number of flow fields considered in the analysis. The results from table 2 reveal that the number of
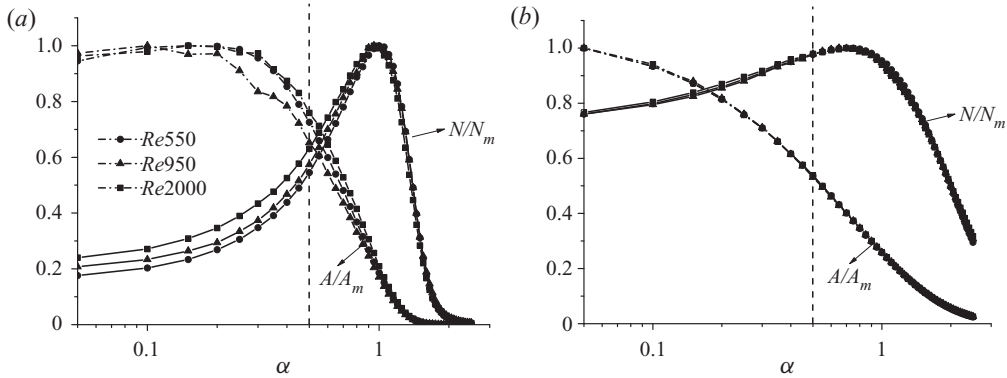
FIGURE 3. Percolation diagrams for the structure identification, (a) NF_s and (b) PF_s. Solid- and dash-dotted lines represent the number fraction (N/N_m) and the area fraction (A/A_m) of the identified structures, respectively. The vertical dashed lines are $\alpha = 0.5$.

Case	N_{PF}	N_{NF}	A_{PF}	A_{NF}	$A_{f,PF}$	$A_{f,NF}$
$Re550$	599 001	291 621	47 386	118 585	0.528	1.322
$Re950$	190 481	98 598	5453	13 427	0.548	1.350
$Re2000$	602 435	479 958	2676	6435	0.565	1.358

TABLE 2. The total number and area of the identified structures. Here, N_{PF} and N_{NF} are the total number of PF_s and NF_s, respectively. Here, A_{PF} and A_{NF} are the total area of PF_s and NF_s, respectively. Here, $A_{f,PF}$ and $A_{f,NF}$ are the area fraction of PF_s and NF_s, respectively.

PF_s is larger than NF_s, but the area of PF_s is smaller than NF_s, regardless of the Reynolds number. This result establishes the first difference between PF_s and NF_s, which will be studied in detail in the following section.

4. Results and discussion

In this section, we dissect the statistical properties of the τ'_x structures, namely, the geometrical characteristics, spatial distribution, population density, fluctuating intensity and correlations with outer motions. Particular attention is paid to the asymmetries between PF_s and NF_s and their relationship with the wall-attached eddies.

4.1. *Geometrical properties of the structures*

The geometrical properties of the structures are characterized by the two length scales, l_x^+ and l_z^+, which are normalized by viscous units. Figures 4(a) and 4(b) show the joint p.d.f.s of l_x^+ and l_z^+ for PF_s and NF_s, respectively. The joint p.d.f.s cover a wide range of l_x^+ and l_z^+, which implies that the skin-friction events are multiscale and the result of the collective effect of motions with different length scales (de Giovanetti *et al.* 2016; Yang & Lozano-Durán 2017; Cho *et al.* 2018; Agostini & Leschziner 2019*a*; Baidya *et al.* 2019; Cheng *et al.* 2019). The mode of the joint p.d.f.s for PF_s and NF_s follows approximately
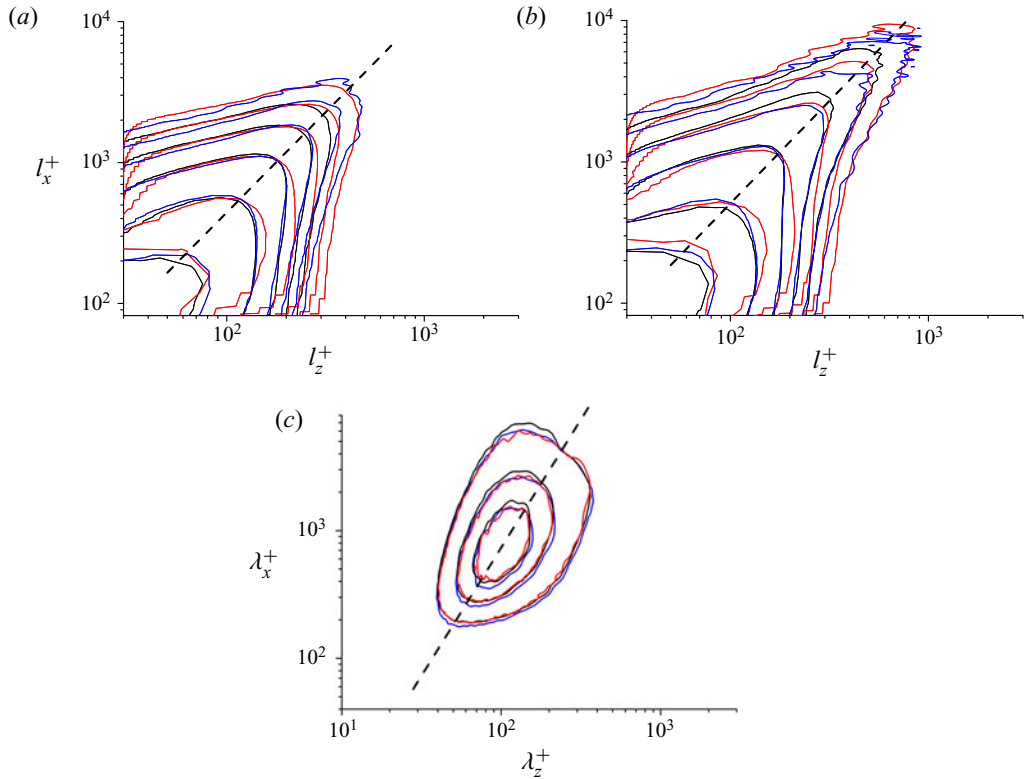
$$l_x^+ = 0.64(l_z^+)^{1.44} \tag{4.1}$$

FIGURE 4. (*a,b*) Joint p.d.f.s of l_z^+ and l_x^+ for PF_s (*a*) and NF_s (*b*). The dashed straight lines in panel (*a*) and panel (*b*) denote $l_x^+ = 0.64(l_z^+)^{1.44}$. All contour levels of the p.d.f.s are logarithmically distributed. (*c*) Two-dimensional premultiplied spectra of u' in the viscous region. The dashed straight lines in panel (*c*) denote $\lambda_x^+ \propto (\lambda_z^+)^2$. Contour lines are 0.25, 0.5 and 0.75 of the maximum. For all figures, black lines denote $Re550$, red lines denote $Re950$ and blue lines denote $Re2000$.

for $l_z^+ \geq 100$. For reference, figure 4(*c*) shows the two-dimensional spectra of u' in the viscous region. The streamwise wavelength (λ_x^+) and the spanwise wavelength (λ_z^+) follows $\lambda_x^+ \propto (\lambda_z^+)^2$, which coincides with the power law between λ_x^+ and λ_z^+ of the u' spectra in the logarithmic region reported by Del Álamo *et al.* (2004). One possible explanation for the nonlinear relationship between λ_x^+ and λ_z^+ (or l_x^+ and l_z^+) is the meandering nature of the near-wall u' structures. At low Reynolds numbers, Jiménez, Del Álamo & Flores (2004) observed a power law relationship between λ_x^+ and λ_z^+ for near-wall streaky structures when taking their meandering nature into account. Some recent studies have reported a linear relationship between λ_x^+ and λ_z^+ at very large Reynolds number. Chandran *et al.* (2017) investigated the two-dimensional spectra of u' in a turbulent boundary layer at $Re_\tau = 26\,000$, and found a linear relationship of $\lambda_x^+ \propto \lambda_z^+$. Therefore, l_x^+ and l_z^+ of the τ_x' structures might also follow a linear relationship at sufficiently high Reynolds numbers.

Under the attached-eddy model framework (Townsend 1976; Perry & Chong 1982) and assuming that wall-attached eddies are space filling, Srinath *et al.* (2018) and Solak & Laval (2018) pointed out that the p.d.f. of l_x^+ should obey $p \propto (l_x^+)^{-2}$. The marginal p.d.f.s of l_x^+ for τ_x' structures is shown in figure 5. It can be seen that asymmetrical features are
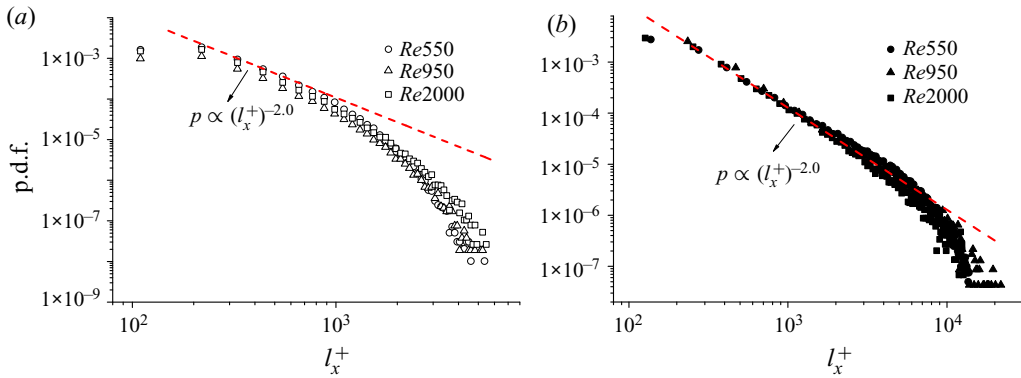
FIGURE 5. Marginal p.d.f.s of l_x^+ for PF_s (a) and NF_s (b). The red dashed lines in figures represent $p \propto (l_x^+)^{-2.0}$.
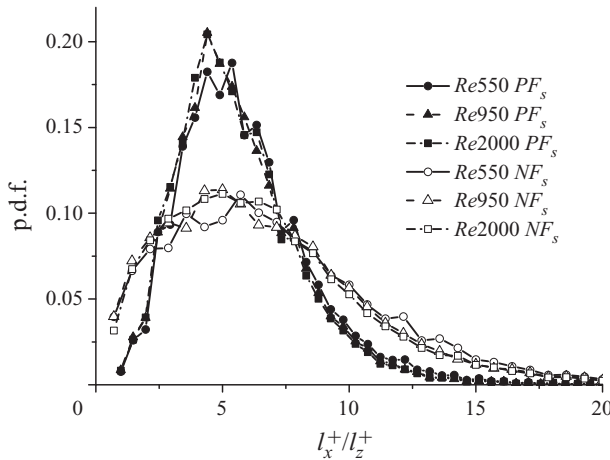

FIGURE 6. Marginal p.d.f.s of l_x^+/l_z^+ for the structures.

exhibited between PF_s and NF_s. For NF_s, the p.d.f.s of l_x^+ approximately follow $p \propto (l_x^+)^{-2}$, which is consistent with the prediction of Srinath *et al.* (2018) and Solak & Laval (2018); whereas for PF_s, the relation is less accurate. This result suggests that NF_s may be the direct outcome of the space-filling wall-attached eddies, which will be analysed in detail in §4.5.

The marginal p.d.f.s of aspect ratio l_x^+/l_z^+ are shown in figure 6. The p.d.f.s of PF_s and NF_s differ in shape, but they are insensitive to the Reynolds number. The p.d.f. profiles of NF_s are flatter than those of PF_s, suggesting that l_x^+/l_z^+ of NF_s is more uniformly distributed. The p.d.f.s reach their maxima at $l_x^+/l_z^+ \approx 5$, regardless of the Reynolds number and the sign of the τ_x' structure.

4.2. *Spatial distribution of the structures*

We investigate next the spatial distribution of τ_x' structures. Let us consider two structures, labelled as i and j. Figure 7 provides a schematic of the two structures. Their relative
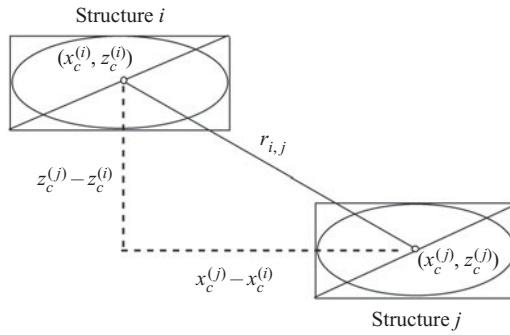
FIGURE 7. The schematic of the distance between two τ'_x structures.

separation in the streamwise and spanwise direction are defined as

$$\delta_x = \frac{x_c^{(j)} - x_c^{(i)}}{d^{(i,j)}} \quad \text{and} \quad \delta_z = \frac{z_c^{(j)} - z_c^{(i)}}{d^{(i,j)}}, \tag{4.2a,b}$$

respectively, where (x_c, z_c) is the centre of the bounding rectangle belonging to the structure i or j, and $d^{(i,j)}$ is the mean diagonal of the two rectangles. The absolute distance of the two structures is defined as

$$r_{i,j} = \sqrt{(x_c^{(j)} - x_c^{(i)})^2 + (z_c^{(j)} - z_c^{(i)})^2}. \tag{4.3}$$

Following the works of Lozano-Durán *et al.* (2012), Dong *et al.* (2017) and Osawa & Jiménez (2018), we only consider structures with $1/2 \le l_z^{(j)}/l_z^{(i)} \le 2$, i.e. the structures sharing similar spanwise size.

Figure 8 shows the joint p.d.f.s of δ_x and δ_z for $Re950$. Similar results are obtained for the other two cases, which are not shown here for brevity. Figure 8 shows that structures tend to be organized side by side along the spanwise direction, while the low probabilities around $\delta_z \approx 0$ indicates that the structures do not overlap along the spanwise direction.

Figure 9 displays the variations of $r_{i,j}^+$ as a function of l_z^+. For $l_z^+ > 100$, NF_s follow the approximately the power law relationship $r_{i,j}^+ \approx 5.3(l_z^+)^{0.8}$, regardless of the Reynolds number, whereas a similar trend is absent for PF_s.

4.3. *Scale-dependent properties of the structures*

In this section we investigate the properties of the τ'_x structures conditioned on l_z^+, including the population density, intensity of τ'_x and marginal p.d.f.s of τ'_x at several selected l_z^+.

The scale-dependent population density is defined as

$$n_d(l_z^+) = \frac{N_i(l_z^+)}{N_F A_w^+}, \tag{4.4}$$

where $N_i(l_z^+)$ is the number of the structures with a given l_z^+, N_F is the number of flow fields used to accumulate statistics and $A_w^+ = 2L_x^+ L_z^+$. Figure 10 shows the distribution of n_d as a function of l_z^+ for all cases. It can be seen that, for NF_s, n_d decays logarithmically with $n_d \propto (l_z^+)^{-2.5}$ when $l_z^+ > 100$; whereas a constant power-law decaying rate is less defined for PF_s. The latter suggests that PF_s and NF_s are distributed in different manners.
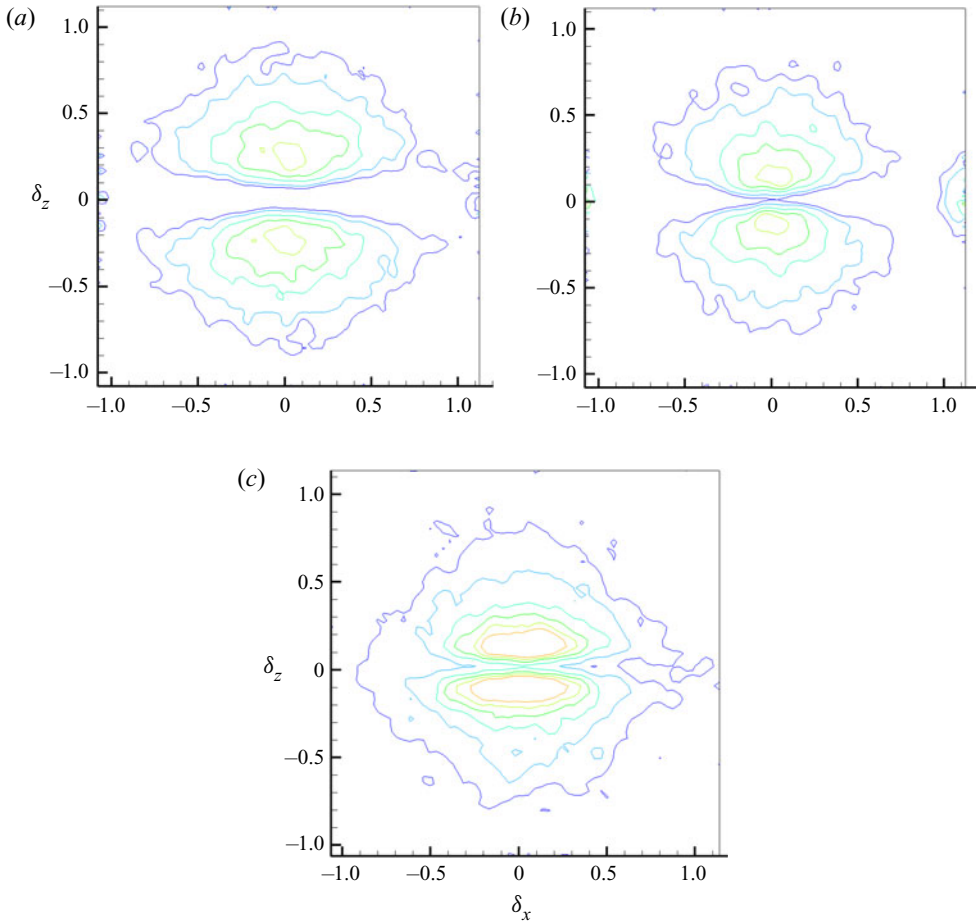
FIGURE 8. Joint p.d.f.s of the relative spacings in $Re950$. (*a*) The closest PF_s relative to a PF_s, (*b*) the closest NF_s relative to a NF_s and (*c*) the closest PF_s relative to a NF_s.
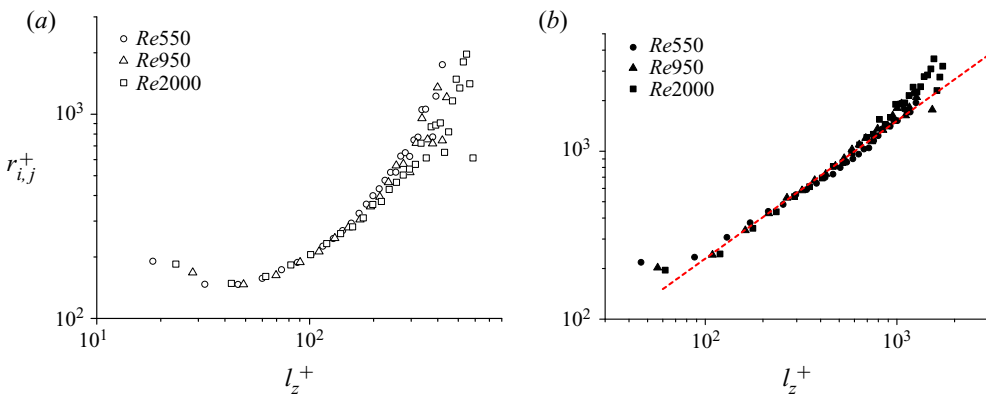

FIGURE 9. Variations of the absolute distance $(r_{i,j}^+)$ as a function of l_z^+. (*a*) PF_s and (*b*) NF_s. The red dashed lines in panel (*b*) denotes $r_{i,j}^+ \approx 5.3(l_z^+)^{0.8}$.
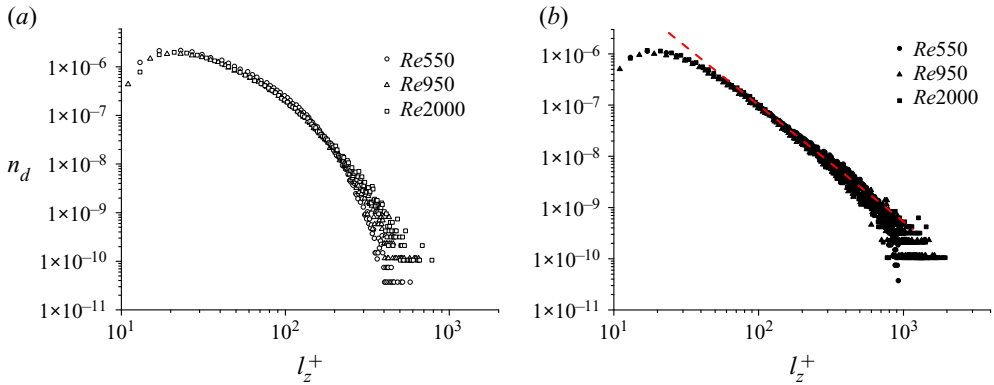
FIGURE 10. Variations of the population density (n_d) as a function of l_z^+. (a) PF_s and (b) NF_s. The red dashed line in panel (b) denotes $n_d \propto (l_z^+)^{-2.5}$.
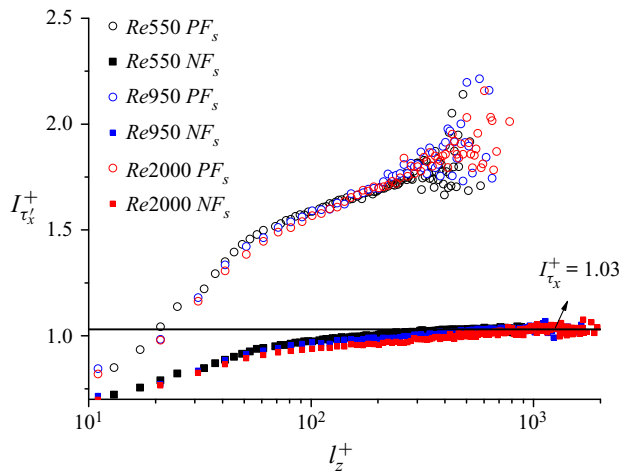

FIGURE 11. Variations of $I_{\tau_x'}^+$ carried by PF_s and NF_s as a function of l_z^+.

The scale-dependent intensity of τ_x' is expressed as

$$I_{\tau_x'}^+(l_z^+) = \sqrt{\frac{1}{N_\tau} \sum_{i=1}^{N_\tau} \left[\frac{\tau_{i,x}'(l_z^+)}{\tau_{x,rms}'} \right]^2}, \tag{4.5}$$

to the structures with a given l_z^+, and $\tau_{i,x}'(l_z^+)$ denotes the instantaneous streamwise wall-shear stress at the ith grid point. In this manner, $I_{\tau_x'}^+(l_z^+)$ represents the intensity of the streamwise wall-shear fluctuations carried by the structures with spanwise size l_z^+. Figure 11 shows the variations of $I_{\tau_x'}^+$ as a function of l_z^+. For both PF_s and NF_s, $I_{\tau_x'}^+$ collapses well, showing the independence of $I_{\tau_x'}^+$ on the friction Reynolds number. For all cases, the expected values of $I_{\tau_x'}^+$ are higher for PF_s than for NF_s, but the former rarely attain size larger than $l_z^+ \approx 300$.

This asymmetrical feature suggest that large-scale outer motions affect mainly the negative skin-friction events. The phenomenon is reminiscent of the asymmetric
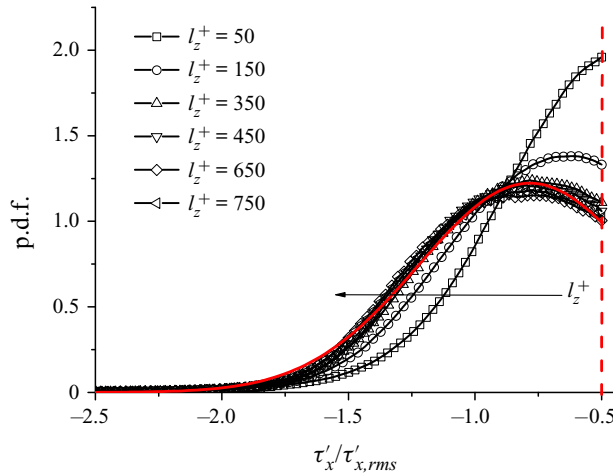
FIGURE 12. The marginal p.d.f.s of $\tau'_x/\tau'_{x,rms}$ for NF_s at several selected l_z^+ by using the case of $Re950$. The red curve denotes a fitting curve by Gaussian function. The vertical dashed line denotes $\tau'_x = -0.5\tau'_{x,rms}$.

modulation of near-wall streamwise velocity fluctuations by positive and negative outer large-scale motions (Agostini & Leschziner 2016a,b, 2018, 2019a). It also implies that the symmetric modelling of positive and negative wall-attached structures by Baidya *et al.* (2019) for the u' spectrum might be improved by accounting for the flow asymmetries.

Another interesting feature revealed by figure 11 is that as l_z^+ increases, the intensity $I_{\tau'_x}^+$ of NF_s converges to a constant value, i.e. $I_{\tau'_x}^+ \approx 1.03$, which suggests that the intensities of large-scale NF_s are independent of l_z^+. The marginal p.d.f.s of $\tau'_x(l_z^+)/\tau'_{x,rms}$ for NF_s at several selected l_z^+ is shown in figure 12 for case $Re950$. Similar trends are observed in the other two cases (not shown). As l_z^+ increases, the p.d.f.s gradually converge to a normal distribution, which is well described by the Gaussian function,

$$p(\zeta)\big|_{l_z^+} = a^{-(\zeta-b)^2/2c^2}, \tag{4.6}$$

where the fitting constants are $a = 1.223$, $b = -0.784$ and $c = 0.44$, and ζ stands for the abscissa in figure 12. The fitting curve is linked to the constant value of $I_{\tau'_x}^+$ in figure 11. The definition of $I_{\tau'_x}^+$ in (4.5) can be rewritten as

$$I_{\tau'_x}^+(l_z^+) = \sqrt{\int_{-\infty}^{-\alpha} \zeta^2 p(\zeta)\big|_{l_z^+} \, d\zeta}. \tag{4.7}$$

Substitution of (4.6) into (4.7) yields

$$I_{\tau'_x}^+(l_z^+) \approx 1.027, \tag{4.8}$$

which is consistent with the constant value ($I_{\tau'_x}^+ \approx 1.03$) shown in figure 11.

The constant value of $I_{\tau'_x}^+$ for large-scale NF_s can be speculated and explained by the properties of the large-scale structures in the near-wall region. Hwang (2016) reported that large-scale u' motions should scale with the inner units in the vicinity of the wall due to viscous effects, which is supported by the measurements of the high-Reynolds-number
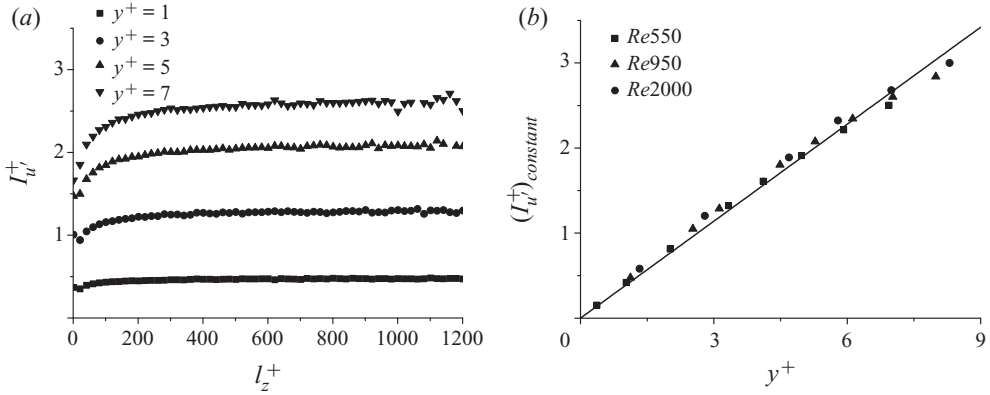
FIGURE 13. (*a*) Variations of $I_{u'}^+$ at several selected y^+ in $Re950$. (*b*) The convergent values of $I_{u'}^+$ (($I_{u'}^+)_{constant}$) with respective to y^+ and the black solid line denotes $(I_{u'}^+)_{constant} = 0.38y^+$.

turbulent boundary layers (Samie *et al.* 2018). Cho *et al.* (2018) further pointed out that this inner scaling is related to the balance between the turbulent transport and dissipation at large scale in the near-wall region. The readers are referred to Hwang (2016) and Cho *et al.* (2018) for more details.

To further investigate the observation of $I_{\tau_x'}^+ \approx constant$, we compute two-dimensional structures of u' at a given y-location using the clustering methodology. The negative near-wall u' structures in the wall-parallel plane are identified following the same approach described in § 3. We have checked that the threshold within $0.4 \leq \alpha \leq 0.7$ has no impact on the conclusions below. Similarly to the definition of $I_{\tau_x'}^+$ in (4.5), we introduce a scale-dependent streamwise turbulence intensity as

$$I_{u'}^+(l_z^+, y^+) = \sqrt{\frac{1}{N_u} \sum_{i=1}^{N_u} \left[\frac{u_i'(l_z^+, y^+)}{u_\tau}\right]^2}, \tag{4.9}$$

where N_u is the total number of the grid points belonging to the negative u' structures with a conditional l_z^+ at y^+, and $u_i'(l_z^+, y^+)$ denotes the negative streamwise velocity fluctuations carried by the ith connected grid point. Analogous to $I_{\tau_x'}^+$, $I_{u'}^+(l_z^+, y^+)$ characterizes the intensity of the streamwise velocity fluctuations of the negative u' structures for a given l_z^+ at y^+.

Figure 13(*a*) displays the variations of $I_{u'}^+$ as a function of l_z^+ at several near-wall locations for $Re950$. Similar trends are observed for the other two cases (not shown here). It can be seen in figure 13(*a*) that as l_z^+ increases, $I_{u'}^+$ tends to be constant with $y^+ \leq 7$. The constant value of $I_{u'}^+$ (denoted by $(I_{u'}^+)_{constant}$) increases with y^+. Figure 13(*b*) displays the variation of $(I_{u'}^+)_{constant}$ as a function of y^+ for all cases. A linear relationship between $(I_{u'}^+)_{constant}$ and y^+ holds for the three Reynolds numbers considered,

$$(I_{u'}^+)_{constant} \approx Cy^+, \tag{4.10}$$

where C is a constant. The results support the dimensional analysis in Cho *et al.* (2018); LSM of u' in the vicinity of the wall tend to follow inner scaling. According to (4.10), we can assume that the streamwise velocity within the large-scale structures of negative u'

follow the relationship

$$\frac{u'|_{l_z^+}}{u_\tau} \approx -Cy^+. \tag{4.11}$$

Additionally, the streamwise wall-shear fluctuations are given by

$$\tau_x' = \mu \frac{\partial u'}{\partial y}, \tag{4.12}$$

and substituting (4.11) into (4.12) yield

$$\frac{|\tau_x'|_{NF_s}}{\rho u_\tau^2} \approx C, \tag{4.13}$$

which indicates that the magnitude of streamwise wall-shear fluctuations carried by large-scale NF_s is independent of l_z^+ and tends to be a constant value, consistent with figure 11.

4.4. *Correlation between τ_x' structures and outer motions*

It is known that the energy-containing motions populating the logarithmic and outer regions leave a 'footprint' on the wall surface (Hutchins *et al.* 2011; Mathis *et al.* 2013; Agostini & Leschziner 2019*a*). Investigating the fluid patterns in the proximity of the wall-shear events can shed light on the generation mechanism of the τ_x' structures. To this end, we calculate the correlation between the τ_x' structures and the energy-containing motions populating the logarithmic and outer regions by

$$R(r_x, y, r_z)|_{l_z} = \frac{E\left[\tau_x'(x_0, 0, z_0)|_{l_z} u'(x_0 + r_x, y, z_0 + r_z)\right]}{\sigma_{\tau_x'}\sigma_{u'}}, \tag{4.14}$$

where E is the expected value, $(x_0, 0, z_0)$ is the reference point, (r_x, y, r_z) represents spatial differences in the streamwise, wall-normal and spanwise direction, respectively, and $\sigma_{\tau_x'}$ and $\sigma_{u'}$ are the standard deviation of τ_x' and u', respectively.

Figure 14 shows the isosurfaces of $R = 0.2$ for PF_s and NF_s with $l_z^+ = 100$ and 300 for case of $Re950$. It is apparent that well-organized streaky structures emerge in the proximity of $\tau_{x'}$ structures. The streaks associated with PF_s are wider and longer than those associated with NF_s. This feature is robust for varying R, l_z^+ and the Reynolds number. If we set both r_x^+ and r_z^+ in (4.14) to zero, then $R(0, y^+, 0)$ (denoted as $R_a(y^+)$ hereafter) represents the conditional correlation just above the target structures. The variations of $R_a(y^+)$ as a function of y^+ and y/h are shown in figure 15. The large-scale τ_x' structures (both PF_s and NF_s) are significantly correlated with u' above the wall. For PF_s, R_a remains positive across the whole channel height when $l_z^+ > 50$; whereas for NF_s, R_a remains positive until the wall-normal distance y_c^+, which increases with l_z^+.

The asymmetry between the correlations of PF_s and NF_s can be interpreted from the perspective of the quadrant decomposition (Wallace 2016). The joint p.d.f.s of u'^+ and v'^+ just above PF_s and NF_s with $l_z^+ = 310$ are displayed in figure 16. It can be seen that at all wall-normal positions, PF_s are mainly associated with the sweep events ($u'^+ > 0$, $v'^+ < 0$), whereas NF_s are strongly correlated with the ejection events ($u'^+ < 0$, $v'^+ > 0$) in the near-wall region ($y^+ \leq 150$). This observation is in line with the profiles of $R_a(y^+)$ shown in figure 15. In this sense, it is reasonable to hypothesize that PF_s are generated by
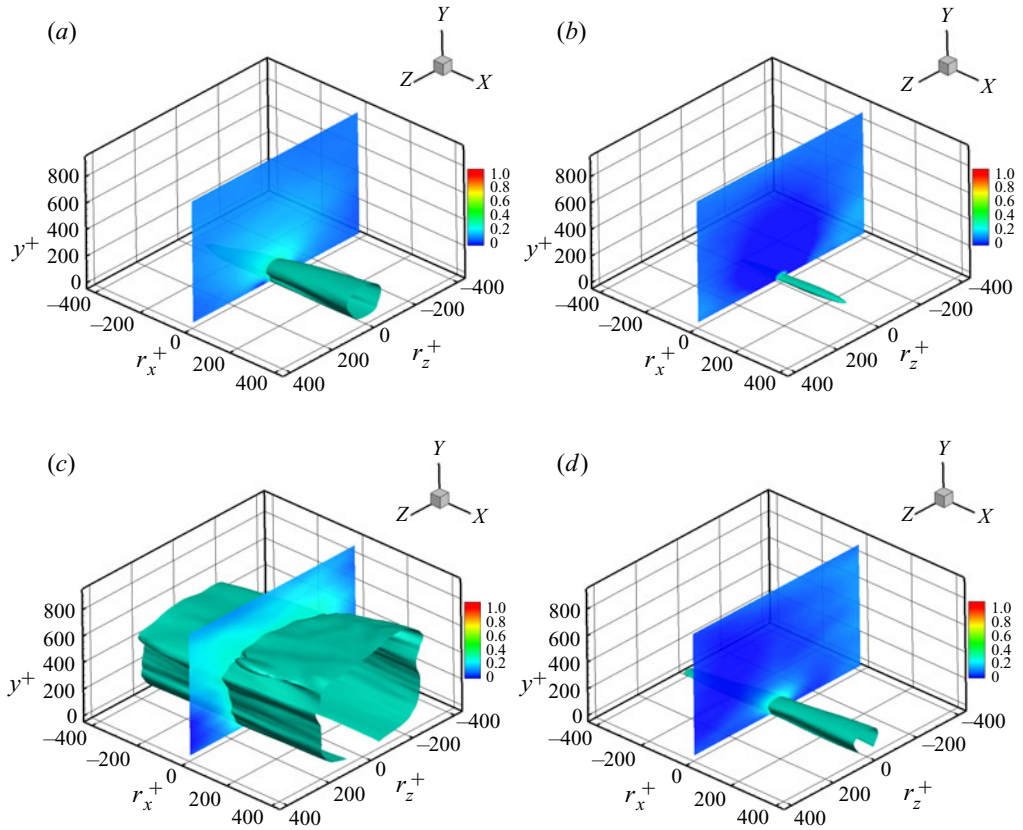
FIGURE 14. (*a,b*) Isosurfaces of $R = 0.2$ for PF_s (*a*) and NF_s (*b*) with $l_z^+ = 100$ in $Re950$. (*c,d*) Isosurfaces of $R = 0.2$ for PF_s (*c*) and NF_s (*d*) with $l_z^+ = 300$ in $Re950$. The colour contours at $r_x^+ = 0$ exhibit the plane-cut correlations.
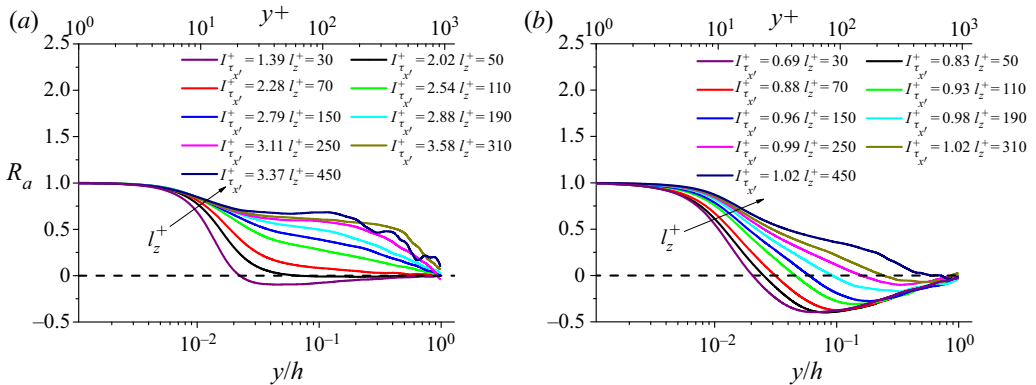

FIGURE 15. Variations of $R_a(y^+)$ as a function of y^+ and y/h for PF_s (*a*) and NF_s (*b*) in $Re950$.

strong sweeps, while NF_s mainly arise from the ejections, consistent with the asymmetry between sweeps and ejections.

Next, we pay attention to the signature of Townsend's attached eddies. The logarithmic decay of the second-order moment of u' is considered to be one of the most compelling
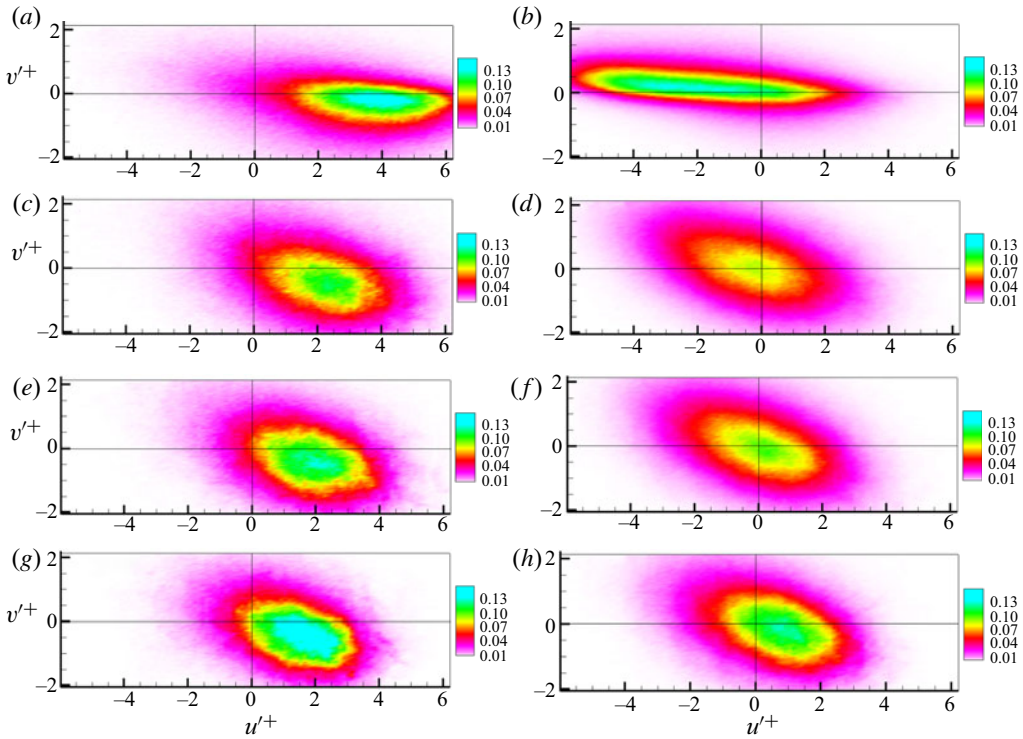
FIGURE 16. Joint p.d.f.s of u'^+ and v'^+ at several y^+, conditioned on PF_s (a,c,e,g) and NF_s (b,d,f,h) with $l_z^+ = 310$ in $Re950$. (a, b) $y^+ = 20$, (c, d) $y^+ = 80$, (e, f) $y^+ = 150$ and (g, h) $y^+ = 250$.

indicators in favour of the attached-eddy model (Marusic *et al.* 2013; Meneveau & Marusic 2013). Inspired by this observation, the streamwise turbulence intensity conditioned on the τ_x' structures is calculated by

$$\overline{u_c'^2}^+ (y^+, l_z^+) = \frac{1}{N_\tau} \sum_{i=1}^{N_\tau} \left[\frac{u_i'(x_0, y^+, z_0)|_{l_z^+}}{u_\tau} \right]^2, \tag{4.15}$$

where $u_i'(x_0, y^+, z_0)|_{l_z^+}$ is the streamwise velocity fluctuation just above the τ_x' structures, with a spanwise length of l_z^+.

Figure 17 shows the variations of $\overline{u_c'^2}^+$ as a function of y^+ and y/h for the structures with several selected l_z^+. The streamwise turbulence intensities of the full channel ($\overline{u'^2}^+$) are also plotted for comparison. Note that the profiles of $\overline{u_c'^2}^+$ are truncated at y_c^+. A remarkable finding is that $\overline{u_c'^2}^+$ decays logarithmically for NF_s similarly to $\overline{u'^2}^+$, but the same trend is not so observed for PF_s.

To quantify the logarithmic decaying of $\overline{u_c'^2}^+$, we define the indicator function, $\Xi = y(\partial \overline{u_c'^2}^+ / \partial y)$. Figure 18 shows the values of Ξ as a function of y^+ for NF_s. The value of Ξ calculated for $\overline{u'^2}^+$ is also included. Compared with the Ξ for the full channel data, slightly better defined plateaus are observed for NF_s in the range of $100 \leq y^+ \leq 0.2h^+$, which spans the conventional logarithmic region (Jiménez 2018; Baars & Marusic 2020b). The wrinkles in figure 18 may be caused by a lack of DNS samples. The observation is striking,
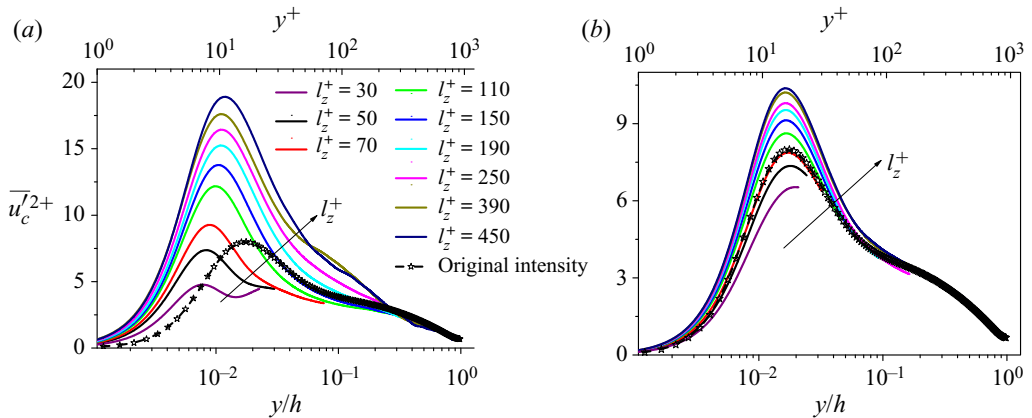
FIGURE 17. Wall-normal variations of $\overline{u_c'^{2+}}$ for PF_s (a) and NF_s (b) in $Re950$ for selected l_z^+. The profile of $\overline{u'^{2+}}$ is included for comparison.

since the logarithmic decay of streamwise turbulence intensity has been only observed at much higher Reynolds numbers (Marusic & Kunkel 2003; Jiménez & Hoyas 2008; Marusic *et al.* 2013; Lee & Moser 2015; Yamamoto & Tsuji 2018). For example, Hultmark *et al.* (2012) reported a logarithmic decay in turbulent pipe flows at $Re_\tau \geq 20\,000$, and Yamamoto & Tsuji (2018) showed the logarithmic decay in the DNS of turbulent channel flows at $Re_\tau = 8000$. Our observations at lower Reynolds numbers underlines the fact that the large-scale NF_s identified in the present study have active connection with the attached eddies populating the logarithmic region. The results are also consistent with Cheng *et al.* (2020), who showed that Townsend's wall-attached eddies are present in wall turbulence at Reynolds numbers that are traditionally considered low.

To further assess the flow properties above the τ_x' structures, the marginal p.d.f.s of u' at $y^+ = 150$ above PF_s and NF_s with $l_z^+ = 310$ are compared with the p.d.f.s for the full channel data in figure 19(*a*). The individual root mean square of u' is used for normalization. It should be noted this wall-normal position is below y_c^+ and located in the logarithmic region. The p.d.f. of u' above NF_s is highly symmetric and follows a Gaussian distribution as that for u' for the full channel; whereas the p.d.f. of u' above PF_s is highly skewed. Similar results are found in the other two Reynolds numbers, which are not shown here for brevity. Bearing in mind that u' should exhibit a Gaussian distribution in the logarithmic region according to the attached-eddy model (Meneveau & Marusic 2013; Marusic & Monty 2019), our results suggest again that NF_s are linked to wall-attached eddies, whereas PF_s are not.

Another consequence of the attached-eddy model is the increase of the inner peaks of the second-order moment of u' as $\ln(Re_\tau)$, which has been validated in previous numerical and experimental studies (Marusic & Kunkel 2003; Hoyas & Jiménez 2006; Meneveau & Marusic 2013; Lee & Moser 2015). By assuming that the inner peaks of the streamwise turbulence intensities are the outcome of the wall-attached eddies residing in the logarithmic region, Meneveau & Marusic (2013) found that the magnitude of the peaks can be predicted as
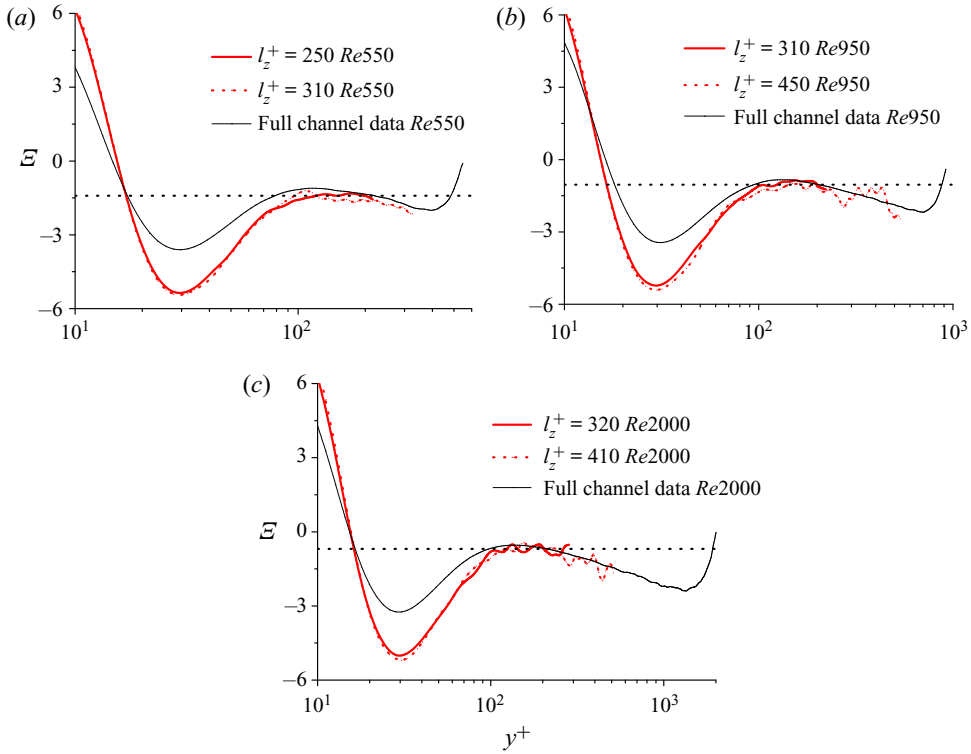
$$\overline{u_m'^2}^+ \sim A_1 \ln Re_\tau, \tag{4.16}$$

FIGURE 18. Wall-normal variations of the indicator function Ξ for NF_s in (*a*) $Re550$, (*b*) $Re950$ and (*c*) $Re2000$.
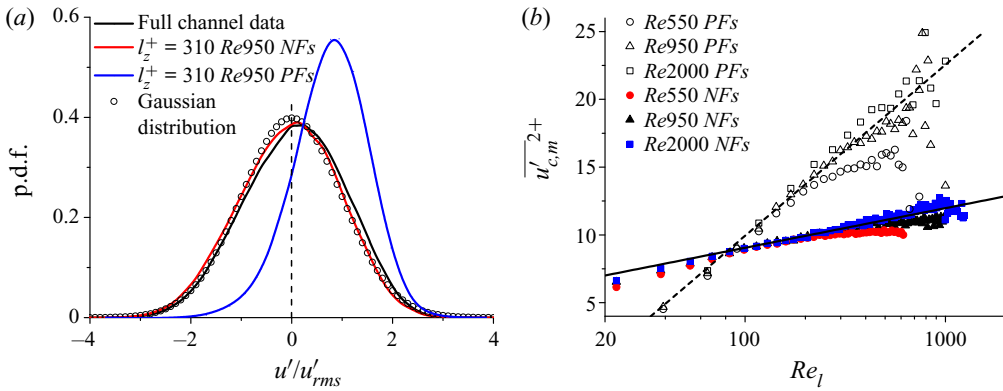

FIGURE 19. (*a*) The marginal p.d.f.s of u'/u'_{rms} at $y^+ = 150$ conditioned on PF_s and NF_s with $l_z^+ = 310$ for $Re950$, comparing with the p.d.f. of the full channel data. (*b*) Variations of the inner peaks $\overline{u'^2_{c,m}}^+$ as a function of l_z^+ for NF_s. The solid and dashed lines denote $\overline{u'^2_{c,m}}^+ \propto 1.27 \ln(Re_l)$ and $\overline{u'^2_{c,m}}^+ \propto 5.48 \ln(Re_l)$, respectively.

where A_1 is the constant in the eddy intensity function in (1.2a). Here, we define a scale-based Reynolds number as

$$Re_l = \frac{l_z \overline{u_{\tau,c}}(l_z)}{\nu},$$ (4.17)

where $\overline{u_{\tau,c}}(l_z)$ is the mean friction velocity carried by the structure with a given l_z, defined by

$$\overline{u_{\tau,c}}(l_z) = \frac{1}{N_\tau} \sum_{i=1}^{N_\tau} u_{\tau,i}|_{l_z},$$ (4.18)

where $u_{\tau,i}|_{l_z}$ denotes the instantaneous friction velocity at the ith grid point belonging to the structures with a given l_z. In this regard, Re_l can be interpreted as a local Reynolds number.

Figure 19(b) aids the examination of the growth rate of the inner peaks $\overline{u_{c,m}'^2}^+$ for PF_s and NF_s. The value of $\overline{u_{c,m}'^2}^+$ for NF_s grows logarithmically with $\ln(Re_l)$ with a slope of 1.27, in the regions of $100 \leq Re_l \leq 200$ for $Re550$, $100 \leq Re_l \leq 400$ for $Re950$ and $100 \leq Re_l \leq 700$ for $Re2000$. The growth rate of 1.27 is in agreement with the value of A_1 in the eddy intensity function (1.2a), as reported in a collection of studies $A_1 \simeq 1.25$–1.26 (Hultmark *et al.* 2012; Marusic *et al.* 2013; Sillero *et al.* 2013; Lozano-Durán & Jiménez 2014a; Marusic, Baars & Hutchins 2017). For PF_s, the peaks increase with $\ln(Re_l)$ with a growth rate of 5.48 for all cases, which is significantly larger than that of NF_s and far from the usual value for A_1 discussed above.

Recently, Hwang (2015) reported that a single attached eddy is composed of two distinct elements. One is a streak carrying streamwise velocity fluctuations and some spanwise velocity fluctuations, another is the short and tall vortical structure containing all the velocity fluctuating components. The scenario is consistent with a series of previous studies (Adrian, Meinhart & Tomkins 2000; Del Álamo *et al.* 2006; Lozano-Durán *et al.* 2012). Seen in this context, it is not difficult to find that the footprint of the streak is the near-wall inactive part of the attached eddy as it does not carry the Reynolds stress. In addition, the long streaks are typically represented as the low-momentum regions (Kim 1999; Adrian *et al.* 2000; Hwang 2015; Lee, Sung & Adrian 2019). Taking these observations, it would be reasonable to view the NF_s as the footprints of the attached eddies populating the logarithmic region, which has been demonstrated from several perspectives in the present study. Finally, we conjecture that the formation of PF_s is caused by the sweep of vortical structures, probably including the second element of a single attached eddy and the 'hairpin vortex packet', a conceptual structure proposed to depict the LSM (Hutchins, Hambleton & Marusic 2005; Adrian 2007; Lee *et al.* 2019). There are three reasons: (i) the correlation of PF_s in figure 14 reaches a higher wall-normal location than that of NF_s with a given l_z^+, which is consistent with the spatial image of a single attached-eddy in the study of Hwang (2015) and the spatial location of LSM; (ii) the correlations of large-scale PF_s in figures 14(c) and 15(a) could be characterized by outer scales, which behave similarly to the scales of LSM (Tomkins & Adrian 2002; Adrian 2007; Baars & Marusic 2020a); and (iii) figure 16 suggests that PF_s are mainly associated with the sweep events far from the wall.

5. Concluding remarks

In the present study, we have utilized a two-dimensional clustering methodology to identify the structures of streamwise wall-shear stress fluctuations (τ_x'). The structures
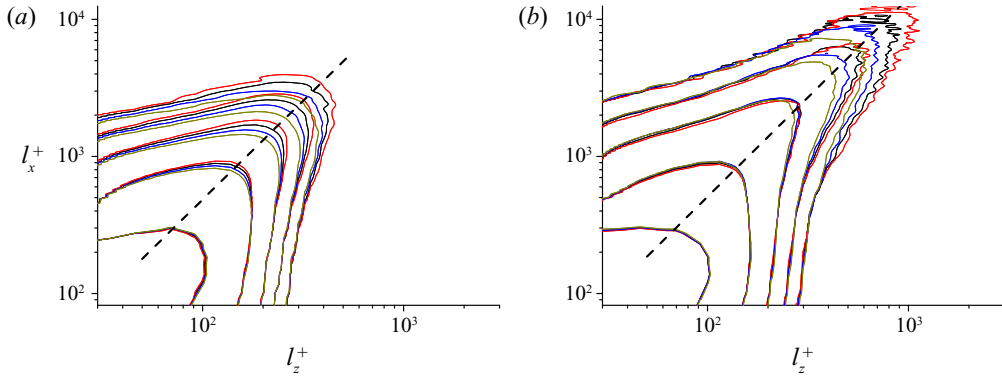
FIGURE 20. Joint p.d.f.s of l_z^+ and l_x^+ for PF_s (a) and NF_s (b). Red lines, $\alpha = 0.4$; black lines, $\alpha = 0.5$; blue lines, $\alpha = 0.6$; and brown lines, $\alpha = 0.7$. The dashed straight lines in panel (a) and panel (b) denote $l_x^+ = 0.64(l_z^+)^{1.44}$. All contour levels of the p.d.f.s are logarithmically distributed.

are classified into positive and negative families, denoted by PF_s and NF_s, respectively, according to their sign. The key findings are summarized below.

(a) The PF_s and NF_s exhibit several asymmetries: (i) PF_s tend to be more fragmented while NF_s are organized in larger scales with approximately constant intensities with respect to their spanwise length scales (l_z^+); (ii) the population densities of PF_s and NF_s decay logarithmically as a function of l_z^+, and the former decay faster; (iii) PF_s are predominantly correlated with the sweep events in the up-wall region, whereas NF_s are strongly impacted by the ejection events; and (iv) the correlations between PF_s and their surrounding streamwise velocities are wider and longer than those associated with NF_s.

(b) The attached eddies populating the logarithmic region are found to be actively connected with large-scale NF_s. The evidence is (i) the p.d.f.s of their lengths (l_x^+) follow the prediction of the attached-eddy model, i.e. $p \propto (l_x^+)^{-2}$; (ii) the streamwise turbulence intensities conditioned on the large-scale NF_s obey a logarithmic wall-normal decay; (iii) the inner peaks increase logarithmically with the local Reynolds numbers at a model-predicted growth rate; and (iv) the streamwise velocity fluctuations conditioned on the large-scale NF_s tend to follow the Gaussian distribution in the logarithmic region.

Finally, the existing theories in the framework of attached-eddy model do not account for the asymmetrical features between PF_s and NF_s (Woodcock & Marusic 2015; Yang & Lozano-Durán 2017). In this regard, the results in the present study may aid the future development of more accurate modelling approaches.
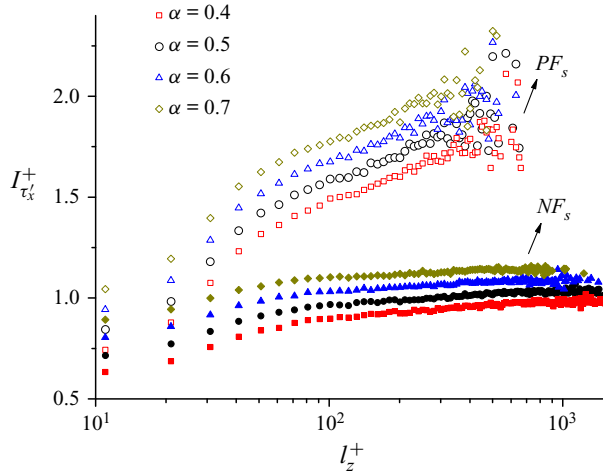
Acknowledgements

FIGURE 21. Variations of the intensity of streamwise wall-shear fluctuations ($I_{\tau_x'}^+$) carried by PF_s and NF_s as a function of l_z^+ over $0.4 \leq \alpha \leq 0.7$ for $Re950$.
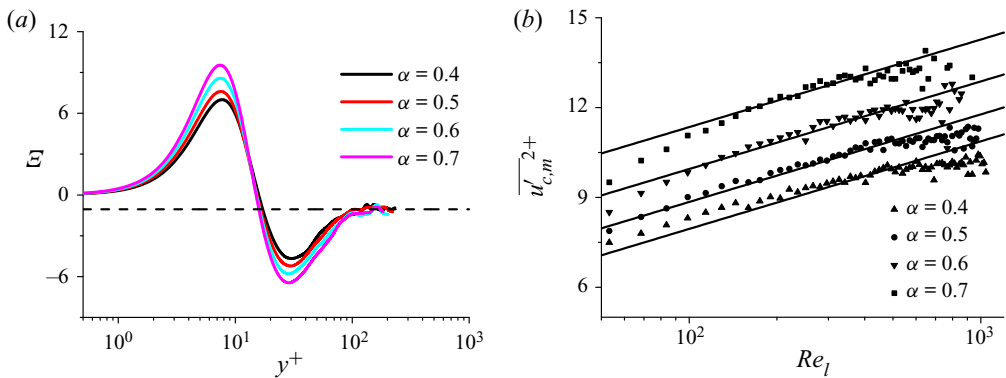

FIGURE 22. (a) Wall-normal variations of the indicator function $\varXi$ for NF_s with $l_z^+ = 310$ over $0.4 \leq \alpha \leq 0.7$ for $Re950$. (b) Variations of the inner peaks $\overline{u_{c,m}'^2}^+$ as a function of l_z^+ over $0.4 \leq \alpha \leq 0.7$ for $Re950$. The black solid lines indicate $\overline{u_{c,m}'^2}^+ \sim 1.27 \ln(Re_l)$.

Declaration of interests

The authors report no conflict of interest.

Appendix. Sensitivity to the threshold α

The influences of the threshold α in (3.1) and (3.2) are examined. Figures 20(a) and 20(b) show the effect of threshold on the joint p.d.f.s of l_x^+ and l_z^+ for $Re950$. The p.d.f.s are well-organized along $l_x^+ = 0.64(l_z^+)^{1.44}$, suggesting that the relation between l_x^+ and l_z^+ of the τ_x' structures does not alter when varying α from 0.4 to 0.7. Figure 21 illustrates the threshold effect on the wall-shear fluctuations carried by PF_s and NF_s for $Re950$. For a

fixed α, the fluctuating intensity of PF_s is pronouncedly larger than that of NF_s at a given l_z^+, and the fluctuating intensity of NF_s converges to constant values at large l_z^+.

Next, we investigate the influence of α on the conditional velocities. The indicator function $\varXi$ for NF_s with $l_z^+ = 310$ over $0.4 \leq \alpha \leq 0.7$ for $Re950$ is displayed in figure 22(a). These profiles are truncated at y_c^+. As seen, the logarithmic decaying in the range of $100 \leq y^+ \leq 0.2h^+$ is not changed with different α. Figure 22(b) shows the variations of the inner peaks $\overline{u_{c,m}'^2}^+$ as a function of Re_l with different α. Although the profiles shift upward with the increase of α, the constant growth rate of 1.27 is still observed in $150 \leq Re_l \leq 500$.

REFERENCES

ABE, H., KAWAMURA, H. & CHOI, H. 2004 Very large-scale structures and their effects on the wall shear-stress fluctuations in a turbulent channel flow up to $Re_\tau = 640$. *Trans. ASME: J. Fluids Engng* **126** (5), 835–843.

ADRIAN, R. J. 2007 Hairpin vortex organization in wall turbulence. *Phys. Fluids* **19** (4), 041301.

ADRIAN, R. J., MEINHART, C. D. & TOMKINS, C. D. 2000 Vortex organization in the outer region of the turbulent boundary layer. *J. Fluid Mech.* **422**, 1–54.

AGOSTINI, L. & LESCHZINER, M. 2016a On the validity of the quasi-steady-turbulence hypothesis in representing the effects of large scales on small scales in boundary layers. *Phys. Fluids* **28** (4), 045102.

AGOSTINI, L. & LESCHZINER, M. 2016b Predicting the response of small-scale near-wall turbulence to large-scale outer motions. *Phys. Fluids* **28** (1), 339–352.

AGOSTINI, L. & LESCHZINER, M. 2018 The impact of footprints of large-scale outer structures on the near-wall layer in the presence of drag-reducing spanwise wall motion. *Flow Turbul. Combust.* **100**, 1037–1061.

AGOSTINI, L. & LESCHZINER, M. 2019a The connection between the spectrum of turbulent scales and the skin-friction statistics in channel flow at $Re_\tau \approx 1000$. *J. Fluid Mech.* **871**, 22–51.

AGOSTINI, L. & LESCHZINER, M. 2019b On the departure of near-wall turbulence from the quasi-steady state. *J. Fluid Mech.* **871**, R1.

ALFREDSSON, P. H., JOHANSSON, A. V., HARITONIDIS, J. H. & ECKELMANN, H. 1988 The fluctuating wall-shear stress and the velocity field in the viscous sublayer. *Phys. Fluids* **31** (5), 1026–1033.

BAARS, W. J. & MARUSIC, I. 2020a Data-driven decomposition of the streamwise turbulence kinetic energy in boundary layers. Part 1. Energy spectra. *J. Fluid Mech.* **882**, A25.

BAARS, W. J. & MARUSIC, I. 2020b Data-driven decomposition of the streamwise turbulence kinetic energy in boundary layers. Part 2. Integrated energy and a_1. *J. Fluid Mech.* **882**, A26.

BAE, H. J., LOZANO-DURÁN, A., BOSE, S. T. & MOIN, P. 2018 Turbulence intensities in large-eddy simulation of wall-bounded flows. *Phys. Rev. Fluids* **3**, 014610.

BAIDYA, R., BAARS, W. J., ZIMMERMAN, S., SAMIE, M., HEARST, R. J., DOGAN, E., MASCOTELLI, L., ZHENG, X., BELLANI, G., TALAMELLI, A. *et al.* 2019 Simultaneous skin friction and velocity measurements in high Reynolds number pipe and boundary layer flows. *J. Fluid Mech.* **871**, 377–400.

CARDESA, J. I., MONTY, J. P., SORIA, J. & CHONG, M. S. 2019 The structure and dynamics of backflow in turbulent channels. *J. Fluid Mech.* **880**, R3.

CHAMBERS, F. W., MURPHY, H. D. & McELIGOT, D. M. 1983 Laterally converging flow. Part 2. Temporal wall shear stress. *J. Fluid Mech.* **127**, 403–428.

CHANDRAN, D., BAIDYA, R., MONTY, J. P. & MARUSIC, I. 2017 Two-dimensional energy spectra in high-Reynolds-number turbulent boundary layers. *J. Fluid Mech.* **826**, R1.

CHAUHAN, K. A., MONKEWITZ, P. A. & NAGIB, H. M. 2009 Criteria for assessing experiments in zero pressure gradient boundary layers. *Fluid Dyn. Res.* **41** (2), 021404.

CHENG, C., LI, W., LOZANO-DURÁN, A. & LIU, H. 2019 Identity of attached eddies in turbulent channel flows with bidimensional empirical mode decomposition. *J. Fluid Mech.* **870**, 1037–1071.

CHENG, C., LI, W., LOZANO-DURÁN, A. & LIU, H. 2020 Uncovering Townsend's wall-attached eddies in low-Reynolds-number wall turbulence. *J. Fluid Mech.* **889**, A29.

CHO, M., HWANG, Y. & CHOI, H. 2018 Scale interactions and spectral energy transfer in turbulent channel flow. *J. Fluid Mech.* **854**, 474–504.

CHOUDHARI, M. M. & KHORRAMI, M. R. 2007 Effect of three-dimensional shear-layer structures on slat cove unsteadiness. *AIAA J.* **45** (9), 2174.

DAVIDSON, P. A., NICKELS, T. B. & KROGSTAD, P.-Å. 2006 The logarithmic structure function law in wall-layer turbulence. *J. Fluid Mech.* **550**, 51–60.

DEL ÁLAMO, J. C., JIMÉNEZ, J. 2003 Spectra of the very large anisotropic scales in turbulent channels. *Phys. Fluids* **15** (6), L41–L44.

DEL ÁLAMO, J. C., JIMÉNEZ, J., ZANDONADE, P. & MOSER, R. D. 2004 Scaling of the energy spectra of turbulent channels. *J. Fluid Mech.* **500**, 135–144.

DEL ÁLAMO, J. C., JIMÉNEZ, J., ZANDONADE, P. & MOSER, R. D. 2006 Self-similar vortex clusters in the turbulent logarithmic region. *J. Fluid Mech.* **561**, 329–358.

DIAZ-DANIEL, C., LAIZET, S. & VASSILICOS, J. C. 2017 Wall shear stress fluctuations: mixed scaling and their effects on velocity fluctuations in a turbulent boundary layer. *Phys. Fluids* **29** (5), 055102.

DONG, S., LOZANO-DURÁN, A., SEKIMOTO, A. & JIMÉNEZ, J. 2017 Coherent structures in statistically stationary homogeneous shear turbulence. *J. Fluid Mech.* **816**, 167–208.

ECKELMANN, H. 1974 The structure of the viscous sublayer and the adjacent wall region in a turbulent channel flow. *J. Fluid Mech.* **65** (3), 439–459.

FAN, Y., CHENG, C. & LI, W. 2019a Effects of the Reynolds number on the mean skin friction decomposition in turbulent channel flows. *Z. Angew. Math. Mech.* **40**, 331–342.

FAN, Y., LI, W. & PIROZZOLI, S. 2019b Decomposition of the mean friction drag in zero-pressure-gradient turbulent boundary layers. *Phys. Fluids* **31** (8), 086105.

FISCHER, M., JOVANOVIĆ, J. & DURST, F. 2001 Reynolds number effects in the near-wall region of turbulent channel flows. *Phys. Fluids* **13** (6), 1755–1767.

FUKAGATA, K., IWAMOTO, K. & KASAGI, N. 2002 Contribution of Reynolds stress distribution to the skin friction in wall-bounded flows. *Phys. Fluids* **14** (11), L73–L76.

GANAPATHISUBRAMANI, B., HUTCHINS, N., MONTY, J. P., CHUNG, D. & MARUSIC, I. 2012 Amplitude and frequency modulation in wall turbulence. *J. Fluid Mech.* **712**, 61–91.

DE GIOVANETTI, M., HWANG, Y. & CHOI, H. 2016 Skin-friction generation by attached eddies in turbulent channel flow. *J. Fluid Mech.* **808**, 511–538.

GOSE, J. W., GOLOVIN, K., BOBAN, M., MABRY, J. M., TUTEJA, A., PERLIN, M. & CECCIO, S. L. 2018 Characterization of superhydrophobic surfaces for drag reduction in turbulent flow. *J. Fluid Mech.* **845**, 560–580.

GROSSE, S. & SCHRÖDER, W. 2009 High Reynolds number turbulent wind tunnel boundary layer wall-shear stress sensor. *J. Turbul.* **10**, N14.

GUALA, M., HOMMEMA, S. E. & ADRIAN, R. J. 2006 Large-scale and very-large-scale motions in turbulent pipe flow. *J. Fluid Mech.* **554**, 521–542.

HOWLAND, M. F. & YANG, X. I. A. 2018 Dependence of small-scale energetics on large scales in turbulent flows. *J. Fluid Mech.* **852**, 641–662.

HOYAS, S. & JIMÉNEZ, J. 2006 Scaling of the velocity fluctuations in turbulent channels up to $Re_\tau = 2003$. *Phys. Fluids* **18** (1), 011702.

HU, R., YANG, X. I. A. & ZHENG, X. 2020 Wall-attached and wall-detached eddies in wall-bounded turbulent flows. *J. Fluid Mech.* **885**, A30.

HU, R. & ZHENG, X. 2018 Energy contributions by inner and outer motions in turbulent channel flows. *Phys. Rev. Fluids* **3** (8), 084607.

HU, Z. W., MORFEY, C. L. & SANDHAM, N. D. 2006 Wall pressure and shear stress spectra from direct simulations of channel flow. *AIAA J.* **44** (7), 1541–1549.

HULTMARK, M., VALLIKIVI, M., BAILEY, S. C. C. & SMITS, A. J. 2012 Turbulent pipe flow at extreme Reynolds numbers. *Phys. Rev. Lett.* **108** (9), 094501.

HUTCHINS, N., HAMBLETON, W. T. & MARUSIC, I. 2005 Inclined cross-stream stereo particle image velocimetry measurements in turbulent boundary layers. *J. Fluid Mech.* **541**, 21–54.

HUTCHINS, N. & MARUSIC, I. 2007 Evidence of very long meandering features in the logarithmic region of turbulent boundary layers. *J. Fluid Mech.* **579**, 1–28.

HUTCHINS, N., MONTY, J. P., GANAPATHISUBRAMANI, B., NG, H. C. H. & MARUSIC, I. 2011 Three-dimensional conditional structure of a high-Reynolds-number turbulent boundary layer. *J. Fluid Mech.* **673**, 255–285.

HWANG, J. & SUNG, H. J. 2018 Wall-attached structures of velocity fluctuations in a turbulent boundary layer. *J. Fluid Mech.* **856**, 958–983.

HWANG, J. & SUNG, H. J. 2019 Wall-attached clusters for the logarithmic velocity law in turbulent pipe flow. *Phys. Fluids* **31** (5), 055109.

HWANG, Y. 2015 Statistical structure of self-sustaining attached eddies in turbulent channel flow. *J. Fluid Mech.* **767**, 254–289.

HWANG, Y. 2016 Mesolayer of attached eddies in turbulent channel flow. *Phys. Rev. Fluids* **1** (6), 064401.

JIMÉNEZ, J. 2018 Coherent structures in wall-bounded turbulence. *J. Fluid Mech.* **842**, P1.

JIMÉNEZ, J., DEL ÁLAMO, J. C. & FLORES, O. 2004 The large-scale dynamics of near-wall turbulence. *J. Fluid Mech.* **505**, 179–199.

JIMÉNEZ, J. & HOYAS, S. 2008 Turbulent fluctuations above the buffer layer of wall-bounded flows. *J. Fluid Mech.* **611**, 215–236.

KARLSSON, R. I. & JOHANSSON, T. G. 1986 LDV measurements of higher order moments of velocity fluctuations in a turbulent boundary layer. In *3rd International Symposium on Applications of Laser Anemometry to Fluid Mechanics* (ed. R. J. Adrian), 12.1.

KAWATA, T. & ALFREDSSON, P. H. 2018 Inverse interscale transport of the Reynolds shear stress in plane Couette turbulence. *Phys. Rev. Lett.* **120** (24), 244501.

KIM, K. C. 1999 Very large-scale motion in the outer layer. *Phys. Fluids* **11** (2), 417–422.

LEE, J. H., SUNG, H. J. & ADRIAN, R. J. 2019 Space time formation of very-large-scale motions in turbulent pipe flow. *J. Fluid Mech.* **881**, 1010–1047.

LEE, M. & MOSER, R. D. 2015 Direct numerical simulation of turbulent channel flow up to $Re_\tau \approx 5200$. *J. Fluid Mech.* **774**, 395–415.

LI, W., FAN, Y., MODESTI, D. & CHENG, C. 2019 Decomposition of the mean skin-friction drag in compressible turbulent channel flows. *J. Fluid Mech.* **875**, 101–123.

LI, W. & LIU, H. 2019 Two-point statistics of coherent structures in turbulent flow over riblet-mounted surfaces. *Acta Mechanica Sin.* **35**, 457–471.

LOZANO-DURÁN, A. & BAE, H. J. 2019 Characteristic scales of Townsend's wall-attached eddies. *J. Fluid Mech.* **868**, 698–725.

LOZANO-DURÁN, A., FLORES, O. & JIMÉNEZ, J. 2012 The three-dimensional structure of momentum transfer in turbulent channels. *J. Fluid Mech.* **694**, 100–130.

LOZANO-DURÁN, A. & JIMÉNEZ, J. 2014a Effect of the computational domain on direct simulations of turbulent channels up to $Re_\tau = 4200$. *Phys. Fluids* **26** (1), 011702.

LOZANO-DURÁN, A. & JIMÉNEZ, J. 2014b Time-resolved evolution of coherent structures in turbulent channels: characterization of eddies and cascades. *J. Fluid Mech.* **759**, 432–471.

MADAVAN, N. K., DEUTSCH, S. & MERKLE, C. L. 1985 Measurements of local skin friction in a microbubble-modified turbulent boundary layer. *J. Fluid Mech.* **156**, 237–256.

MARUSIC, I. 2001 On the role of large-scale structures in wall turbulence. *Phys. Fluids* **13** (3), 735–743.

MARUSIC, I., BAARS, W. J. & HUTCHINS, N. 2017 Scaling of the streamwise turbulence intensity in the context of inner-outer interactions in wall turbulence. *Phys. Rev. Fluids* **2** (10), 100502.

MARUSIC, I. & KUNKEL, G. J. 2003 Streamwise turbulence intensity formulation for flat-plate boundary layers. *Phys. Fluids* **15** (8), 2461–2464.

MARUSIC, I., MATHIS, R. & HUTCHINS, N. 2010 Predictive model for wall-bounded turbulent flow. *Science* **329** (5988), 193–196.

MARUSIC, I. & MONTY, J. P. 2019 Attached eddy model of wall turbulence. *Annu. Rev. Fluid Mech.* **51**, 49–74.

MARUSIC, I., MONTY, J. P., HULTMARK, M. & SMITS, A. J. 2013 On the logarithmic region in wall turbulence. *J. Fluid Mech.* **716**, R3.

MATHIS, R., HUTCHINS, N. & MARUSIC, I. 2009 Large-scale amplitude modulation of the small-scale structures in turbulent boundary layers. *J. Fluid Mech.* **628**, 311–337.

MATHIS, R., MARUSIC, I., CHERNYSHENKO, S. I. & HUTCHINS, N. 2013 Estimating wall-shear-stress fluctuations given an outer region input. *J. Fluid Mech.* **715**, 163–180.

MENEVEAU, C. & MARUSIC, I. 2013 Generalized logarithmic law for high-order moments in turbulent boundary layers. *J. Fluid Mech.* **719**, R1.

MIZUNO, Y. & JIMÉNEZ, J. 2011 Mean velocity and length-scales in the overlap region of wall-bounded turbulent flows. *Phys. Fluids* **23** (8), 085112.

MODESTI, D., PIROZZOLI, S., ORLANDI, P. & GRASSO, F. 2018 On the role of secondary motions in turbulent square duct flow. *J. Fluid Mech.* **847**, R1.

MOISY, F. & JIMÉNEZ, J. 2004 Geometry and clustering of intense structures in isotropic turbulence. *J. Fluid Mech.* **513**, 111–133.

MOURI, H. 2017 Two-point correlation in wall turbulence according to the attached-eddy hypothesis. *J. Fluid Mech.* **821**, 343–357.

NAGIB, H. M., CHAUHAN, K. A. & MONKEWITZ, P. A. 2007 Approach to an asymptotic state for zero pressure gradient turbulent boundary layers. *Phil. Trans. R. Soc. Lond.* A **365** (1852), 755–770.

NICKELS, T. B., MARUSIC, I., HAFEZ, S. & CHONG, M. S. 2005 Evidence of the k_1^{-1} law in a high-Reynolds-number turbulent boundary layer. *Phys. Rev. Lett.* **95** (7), 074501.

ÖRLÜ, R. & SCHLATTER, P. 2011 On the fluctuating wall-shear stress in zero pressure-gradient turbulent boundary layer flows. *Phys. Fluids* **23** (2), 021704.

OSAWA, K. & JIMÉNEZ, J. 2018 Intense structures of different momentum fluxes in turbulent channels. *Phys. Rev. Fluids* **3**, 084603.

PAN, C. & KWON, Y. 2018 Extremely high wall-shear stress events in a turbulent boundary layer. *J. Phys.: Conf. Ser.* **1001**, 012004.

PERRY, A. E. & CHONG, M. S 1982 On the mechanism of wall turbulence. *J. Fluid Mech.* **119** (119), 173–217.

PERRY, A. E., HENBEST, S. & CHONG, M. S. 1986 A theoretical and experimental study of wall turbulence. *J. Fluid Mech.* **165**, 163–199.

PERRY, A. E. & MARUSIC, I. 1995 A wall-wake model for the turbulence structure of boundary layers. Part 1. Extension of the attached eddy hypothesis. *J. Fluid Mech.* **298** (298), 361–388.

RENARD, N. & DECK, S. 2016 A theoretical decomposition of mean skin friction generation into physical phenomena across the boundary layer. *J. Fluid Mech.* **790**, 339–367.

ROSENFELD, A. & PFALTZ, J. L. 1966 Sequential operations in digital picture processing. *J. ACM* **13** (4), 471–494.

SAMIE, M., MARUSIC, I., HUTCHINS, N., FU, M. K., FAN, Y., HULTMARK, M. & SMITS, A. J. 2018 Fully resolved measurements of turbulent boundary layer flows up to $Re_\tau = 20\,000$. *J. Fluid Mech.* **851**, 391–415.

SCHLATTER, P. & ÖRLÜ, R. 2010 Assessment of direct numerical simulation data of turbulent boundary layers. *J. Fluid Mech.* **659**, 116–126.

SILLERO, J. A., JIMÉNEZ, J. & MOSER, R. D. 2013 One-point statistics for turbulent wall-bounded flows at Reynolds numbers up to $\delta^+ \approx 2000$. *Phys. Fluids* **25** (10), 105102.

SOLAK, I. & LAVAL, J. 2018 Large-scale motions from a direct numerical simulation of a turbulent boundary layer. *Phys. Rev.* E **98** (3), 033101.

SRINATH, S., VASSILICOS, J., CUVIER, C., LAVAL, J., STANISLAS, M. & FOUCAUT, J. 2018 Attached flow structure and streamwise energy spectra in a turbulent boundary layer. *Phys. Rev.* E **97** (5), 053103.

TOMKINS, C. D. & ADRIAN, R. J. 2002 Spanwise structure and scale growth in turbulent boundary layers. *J. Fluid Mech.* **490** (490), 37–74.

TOWNSEND, A. A. 1976 *The Structure of Turbulent Shear Flow*, 2nd edn. Cambridge University Press.

WALLACE, J. M 2016 Quadrant analysis in turbulence research: history and evolution. *Annu. Rev. Fluid Mech.* **48**, 131–158.

WARK, C. E. & NAGIB, H. M. 1991 Experimental investigation of coherent structures in turbulent boundary layers. *J. Fluid Mech.* **230**, 183–208.

WOODCOCK, J. D. & MARUSIC, I. 2015 The statistical behaviour of attached eddies. *Phys. Fluids* **27** (1), 97–120.

WU, X., BALTZER, J. R. & ADRIAN, R. J. 2012 Direct numerical simulation of a 30R long turbulent pipe flow at $R^+ = 685$: large-and very large-scale motions. *J. Fluid Mech.* **698**, 235–281.

YAMAMOTO, Y. & TSUJI, Y. 2018 Numerical evidence of logarithmic regions in channel flow at $Re_\tau = 8000$. *Phys. Rev. Fluids* **3** (1), 012602.

YANG, X. I. A. & LOZANO-DURÁN, A. 2017 A multifractal model for the momentum transfer process in wall-bounded flows. *J. Fluid Mech.* **824**, R2.

YAO, J., CHEN, X. & HUSSAIN, F. 2018 Drag control in wall-bounded turbulent flows via spanwise opposed wall-jet forcing. *J. Fluid Mech.* **852**, 678–709.

YAO, J. & HUSSAIN, F. 2019 Supersonic turbulent boundary layer drag control using spanwise wall oscillation. *J. Fluid Mech.* **880**, 388–429.

YOON, M., AHN, J., HWANG, J. & SUNG, H. J. 2016 Contribution of velocity-vorticity correlations to the frictional drag in wall-bounded turbulent flows. *Phys. Fluids* **28** (8), 081702.

ZHANG, Y., CHEN, H., WANG, K. & WANG, M. 2017 Aeroacoustic prediction of a multi-element airfoil using wall-modeled large-eddy simulation. *AIAA J.* **55**, 4219–4233.